



Contents lists available at ScienceDirect

Chemical Engineering Journal

journal homepage: www.elsevier.com/locate/cej

Effects of dielectric particles on non-oxidative coupling of methane in a dielectric barrier discharge plasma reactor

Juchan Kim^a, Jaekwon Jeoung^a, Jonghyun Jeon^a, Jip Kim^a, Young Sun Mok^b, Kyoung-Su Ha^{a,*}

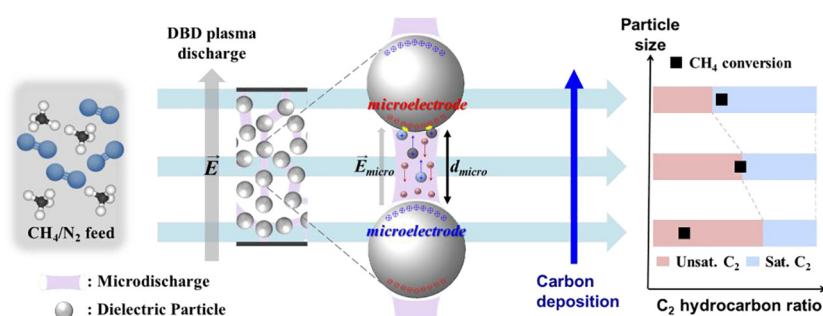
^a Department of Chemical and Biomolecular Engineering, Sogang University, 35 Baekbeom-ro, Mapo-gu, Seoul 04107, Republic of Korea

^b Department of Chemical and Biological Engineering, Jeju National University, Jeju 63243, Republic of Korea

HIGHLIGHTS

- The methane conversion shows its maximum in terms of particle size.
- The concept of microelectrodes explains the existence of maximum conversion.
- By adjusting particle size, selectivity can be controlled without catalyst.
- In terms of coke formation, non-porous silica particles are favored.
- Coke is more produced when large particles are used.

GRAPHICAL ABSTRACT



ARTICLE INFO

Keywords:

Methane
Coupling
Plasma
Dielectric barrier discharge
Ordered mesoporous material

ABSTRACT

A dielectric barrier discharge (DBD) plasma reactor was employed for non-oxidative coupling of methane. The coupling reaction in the DBD plasma bed was conducted near atmospheric pressure and room temperature. In the bed, dielectric materials such as ordered mesoporous silica (KIT-6), sea sand silica, and $\alpha\text{-Al}_2\text{O}_3$ were employed. This non-catalytic reaction system could successfully activate C–H bond to produce methyl radicals and light hydrocarbons without additional thermal energy and oxidant molecules. The gap distance between dielectric particles was determined by their sizes, which was experimentally shown. The effects of gap distance were found significant on the conversion and the selectivity. The existence of maximum conversion at a specific gap distance was experimentally observed and could be described successfully by using a newly developed concept of micro-electrodes. Based on the concept, the minimum threshold electric potential difference between the dielectric particles could be successfully estimated, where the conversion was shown to be maximized. Furthermore, it seemed quite possible to control the compositions of ethane, ethylene, and acetylene by properly adjusting the size or the gap distance of particles.

1. Introduction

The conversion of methane into more valuable hydrocarbons and fuels is one of the most important technologies since methane is a primary component in natural gas resources. There has been lots of research efforts to harness the abundant reservoirs of natural gas by

using efficient catalysts and various conversion technologies. Due to economic reasons, relatively large-sized gas fields have been developed and utilized for gas-to-liquids [1], methanol-to-olefin [2], methanol synthesis [3], dimethyl ether synthesis [4,5] and so on. Unfortunately, those technologies are involved with energy-intensive steps such as gasification and reforming, and they are usually conducted at a very

* Corresponding author.

E-mail address: philoseus@sogang.ac.kr (K.-S. Ha).

<https://doi.org/10.1016/j.cej.2018.09.057>

Nomenclature

d_{micro}	gap distance between two micro-electrodes
$d_{\text{min,micro}}$	minimum gap distance between two micro-electrodes
γ	second Townsend ionization coefficient; secondary electron emission coefficient of micro-cathode
σ	collision cross-sectional area of the gas molecule
E_{micro}	: electric field strength between two micro-electrodes
U_i	ionization potential of the gas molecule
k_B	Boltzmann constant

T	gas temperature
P	gas pressure
A	ionization characteristic constant of the gas molecule. (Equivalent to $\frac{\sigma}{k_B T}$)
B	ionization characteristic constant of the gas molecule. (Equivalent to $\frac{U_i \sigma}{k_B T}$)
$\Delta V_{B,\text{micro}}$	threshold electric potential difference between micro-electrodes to initiate plasma discharges.

high temperature. The severe reaction conditions may limit the choice of reactor materials and reaction catalysts. This situation makes it difficult to reach optimal reaction condition and prepare the best design. Regarding typical non-oxidative coupling reactions of methane to produce C2 chemicals, those reactions in conventional thermochemical reactors usually require a very high temperature (over 1000 °C) to thermally activate C–H bond to produce methyl radicals. Among them, BASF process uses a thermal pyrolysis technique [6] while Huels arc process [7] utilizes high temperature arc plasma to activate and couple methane molecules. Even with catalysts and oxygen co-reactants, at least 800 °C temperature is required to produce C2 chemicals (mostly ethylene and ethane) through the oxidative coupling of methane (OCM), one of the most representative and well-studied conversion technologies [8,9]. Although this technology shows relatively high yields for C2 chemicals, it suffers from the high exothermicity of OCM reaction and the separation burden due to air separation unit for the supply of pure oxygen and the production of pure products [10]. To avoid such energy-intensive conversions, costly separation units, and high operating cost, non-traditional conversion technologies using various energy sources minimizing external thermal heat flows have been recently drawing much attention. Among them, a non-thermal plasma technology has been intensively and extensively studied recently since it directly and efficiently utilizes accelerated electrons and ions to activate the C–H bonds of methane molecules at relatively low temperature without heating all the reaction medium in the bed up to an elevated temperature. Under the non-thermal plasma reaction system, electron temperature is increased up to ~20000 K and the electrons mainly contribute to the reaction. However, the temperature of the bulk including positively charged ions and neutral molecules is close to room temperature. For these reasons, this kind of plasma is regarded as the non-thermal, non-equilibrium plasma (i.e., electron temperature > > gas temperature) [11,12].

For example, the first ozone generation by a non-thermal dielectric barrier discharge (DBD) plasma method was introduced in the middle of 19th century [13]. The ozone has been commercially produced by using the similar DBD technique nowadays [14,15]. Norsic et al. researched methanol oxidation by a DBD plasma combined with MnO₂-CuO based catalysts [16]. The removal of NO_x chemicals using non-thermal plasma method has been studied [17–20]. Also, the removal of SO_x and VOC has been studied by a DBD plasma and non-thermal plasma techniques [21–25]. Recently, the conversion methods by plasma have been reported to produce valuable products. Ozkan et al. [26], Rahmani et al. [27], and Yap et al. [28] introduced dry reforming of methane method to produce synthesis gas and hydrogen by using DBD plasma. Wang et al. reported a steam-enhanced dry reforming technique in a DBD plasma reactor [29]. Liu et al. researched a low temperature plasma to produce light hydrocarbons with catalyst and reported non-oxidative reaction pathways including catalytic conversion [30]. They explained that methane could be converted into methyl radical by reacting with hydrogen radical or electron having over 10 eV, followed by subsequent reactions such as coupling reactions. There have been reported about experimental and analytical evidences of the reactive species which could be generated under the non-

equilibrium methane discharge. For example, by employing a tunable infrared diode laser absorption spectroscopy (IR-TDLAS) and an ultraviolet transmission spectroscopy, Lombardi et al. quantitatively detected the methyl (CH₃) radical [31]. Nozaki et al. performed optical emission spectroscopic measurement for rotational and vibrational state of excited CH(A²Δ) radical in a packed-bed dielectric barrier discharge reactor. They confirmed that the rotational equilibrium of excited CH(A²Δ) is sufficiently established within radiative lifetime (2–3 ns) [32]. Similar approach with TiO₂ and MgO/Al₂O₃ catalyst pellets ranging from 0.25 to 1.75 mm was published more recently [33], and they argued that the smaller catalyst pellets seemed to stabilize the radical intermediates and enhance the surface interaction between the reacting species. They added that this led to increased methane conversion and hydrocarbons selectivity as well. It was pointed out that the pellets refract the electric field, making it non-uniform and stronger than the externally applied field by a factor of 10–250 [11]. According to the literatures [34–36], when the packed dielectric particles polarized due to the applied voltage, the local electric field was enhanced near at the contact points between the beads. Moreover, the electron energies were increased, which produce more energetic electrons and the reactive species for the reaction. It leads to the higher reactant conversion compared to the unpacked DBD reactor. Regarding the packed-bed reactor with non-thermal plasma, Butterworth et al. pointed out that the small particles in the bed increased the density of contact points initiating discharges, the interfacial area between solid and plasma for heterogeneous catalytic reaction, and the volume fraction of gas-plasma contacts [37]. It was also added that the surface discharge might become increasingly dominant over microdischarges in the packed-bed with small particles. The demerits were also pointed out that smaller particles may inhibit the formation of a discharge in the void spaces [38], increase pressure drop through the bed, and increase the loss rate of reactive species and electrons.

In this work, we use a dielectric barrier discharge (DBD) plasma reactor for non-oxidative coupling of methane. By doing so, a direct non-catalytic conversion from methane into C2–C4 hydrocarbons at room temperature is to be elucidated. We experiment and study the effects of particle size, far below the conventional pellet size (ca. 1 mm–10 mm). The existence of maximum methane conversion is analyzed experimentally and the phenomenon could be successfully described by using a newly developed micro-electrode concept. The control of product selectivity is found in terms of material species, porosity and particle size.

2. Experimental

2.1. Preparation of the material

The α-Al₂O₃ in this study was prepared by thermal treatment of γ-Al₂O₃ (Sigma-Aldrich, USA) at 1000 °C for 8 h. Sea sand was purchased from Fisher Chemical, USA. Considering typical recipe [39], KIT-6 in this study was prepared by a slightly modified method. 6 g of triblock copolymer P123 (EO₂₀PO₇₀EO₂₀, MW = 5800 g/mol, Sigma-Aldrich,

USA) was dissolved in the mixture of 217.64 g of deionized water and 11.16 g of HCl (37%, Sigma-Aldrich, USA) at 35 °C with agitation to form a homogeneous solution. 6 g of 1-butanol (Sigma-Aldrich, USA) was then added to the mixture and stirred for 2 h. 12.77 g of silica precursor, tetraethoxysilane (Alfa Aesar, USA) was then slowly added to the mixture and stirred for 24 h. The mixture was then placed to a polypropylene bottle and hydrothermally treated at 100 °C for 24 h, followed by 3 times of washing with deionized water and ethanol. Then, the washed sample was placed to 110 °C oven to dry for 24 h. The dried sample was calcined at 550 °C for 5 h. All materials were separated to three groups (S, M, and L; $0 < S < 53 < M < 100 < L < 150 \mu\text{m}$) in terms of particle size by using stainless steel sieves.

2.2. Material characterization

Transmission electron microscopy (TEM) images and energy dispersive X-ray spectroscopy (EDS) results of fresh $\alpha\text{-Al}_2\text{O}_3$, spent $\alpha\text{-Al}_2\text{O}_3$, fresh sea sand, spent sea sand, fresh KIT-6, and spent KIT-6 were acquired with a JEM-2100F field emission transmission electron microscope under a working voltage of 200 kV (FE-TEM, USA). Scanning electron microscopy (SEM) images were obtained using a scanning electron microscope (JSM-6010LA, JEOL, Japan). Au coating was applied onto all samples via ion sputtering (Sputter Coater 108auto, Cressington Scientific Instruments Ltd., UK) before the SEM imaging was conducted. X-ray diffraction (XRD) analyses were performed using a Rigaku D/Max-2500 V/PC diffractometer (Japan) with a Cu K α radiation (40 kV, 200 mA, $\lambda = 0.154 \text{ nm}$) with 2θ ranging from 10° to 80° for the $\alpha\text{-Al}_2\text{O}_3$ and the sea sand samples, and 10° to 50° for the KIT-6 samples. Small angle X-ray scattering (SAXS) analyses for the KIT-6 samples were performed using a Rigaku D/Max-2500 V/PC diffractometer (Japan) with a Cu K α radiation (50 kV, 250 mA, $\lambda = 0.154 \text{ nm}$). N_2 physisorption measurements for the fresh KIT-6 samples were conducted at 77 K with an ASAP 2020 analyzer (Micromeritics, Inc., USA). Before the measurements, the fresh and the spent samples were degassed at 573 K for 12 h under vacuum. Fourier-transform infrared spectroscopy (FT-IR) analyses were performed by using a Nicolet iS50 spectrometer (Thermo Fisher Scientific, Inc., USA).

After the reaction in the plasma bed, the total weight of coke formed on the samples was measured by conducting a thermogravimetric analysis (TGA). Specifically, the samples were heated from 40 °C to 800 °C with a ramping speed of $20^\circ\text{C min}^{-1}$ under air (Q50, TA Instruments, USA).

2.3. Packed-bed DBD plasma reactor and activity test

Non-oxidative methane coupling reaction was conducted in a lab-made packed-bed DBD plasma reactor system at atmospheric pressure and near room temperature. The schematic diagram of the employed DBD plasma reactor system is illustrated in Fig. S1. The volumetric flow rate of methane mixture ($\text{CH}_4:\text{N}_2 = 1:1$) was 40 standard cubic centimeter per min (sccm), and the total time for the reaction was 1000 min. An alumina tube of 6 mm internal diameter and 2 mm thickness was used as dielectric barrier for the plasma bed. A 3-mm-diameter stainless steel rod was used as powered electrode, and a steel wire was used as ground electrode. The 150-mm-long discharge zone was covered with the ground electrode. The discharge gap between the inner surface of the alumina tube and the high voltage electrode was 1.5 mm, and the volume of this plasma discharge region was fixed as 3.181 cm^3 and the space velocity (SV) based on the volume was set at 754.5 h^{-1} . Each dielectric packing material was fully packed in this region. A sinusoidal AC power supply (0–220 V, 60–1000 Hz) was connected to a transformer (0–20 kV, 1000 Hz), and this electrical system continuously applied a high voltage to the plasma bed. The applied voltage and the frequency to the plasma bed were fixed as 15 kV and 1 kHz, respectively. A capacitor with capacitance of $1 \mu\text{F}$ was connected in series between the plasma bed and the ground. The voltage applied to the

plasma bed was measured by employing a high voltage probe (1000:1, P6015A, Tektronix). The voltage across the $1 \mu\text{F}$ capacitor was measured by employing a voltage probe (10:1, P6100, Tektronix) connected to each side of the capacitor. A current probe (TCP202, Tektronix) was connected on the grounded electrode to evaluate the current profile across the DBD plasma bed. The probes were connected to a digital oscilloscope (TDS 3012C, Tektronix). The accumulated electric charge in the plasma bed was calculated by multiplying the voltage across the capacitor and the capacitance of the capacitor ($1 \mu\text{F}$). The discharge power was calculated in Table 2 by Lissajous method with measured voltage (V) and charge (Q) Lissajous plot as illustrated in Fig. S4 [40].

During the reaction, the reactor temperature was measured with IR temperature detector. The temperature at inlet was nearly room temperature and the temperature of the bed was monitored. The maximum temperature was observed in the center region of the reactor as 100 °C. The observed temperatures in other regions were below 100 °C and most were close to room temperature. An external insulation or an oven was not used in this reactor system.

The effluent gas from the plasma bed was analyzed by an on-line gas chromatograph (6500GC Young Lin Instrument Co., Korea) employing a Porapak-N and a Molecular Sieve 13X columns connected with a thermal conductivity detector (TCD) and a GS-GasPro column connected with a flame ionization detector (FID). H_2 , N_2 , and CH_4 in the effluent were detected by using the TCD. CH_4 , C_2H_2 , C_2H_4 , C_2H_6 , C_3H_6 , C_3H_8 , 1- C_4H_8 , and n- C_4H_{10} in the effluent were detected by using the FID. The energy yield of product i (Y_i) which is defined as ratio of the mass flow rate of product i and the corresponding discharge power was rigorously calculated in Table 2 [41].

3. Results and discussion

3.1. The tested samples and their characteristics

The effect of packed particles was investigated. The $\alpha\text{-Al}_2\text{O}_3$, sea sand, and KIT-6 were employed. By doing so, several kinds of comparison studies were conducted; a comparison between blank and packed-bed, a comparison between alumina ($\alpha\text{-Al}_2\text{O}_3$) and silica (sea sand), and a comparison between nonporous (sea sand) and porous material (KIT-6).

For each material, 3 groups with different sizes were prepared and those groups were named S, M, and L as described previously as shown in Table 1. The images by SEM analyses were given in Fig. 1. And the distributions of gap between the particles were shown in Fig. 2 and Table 1, where the gap was found highly related to the size of particles. In the cases of $\alpha\text{-Al}_2\text{O}_3$ particles, the mean values of gap between S, M and L particles were measured 4.30, 4.73, and $9.87 \mu\text{m}$, respectively. In the cases of the sea sand and KIT-6 particles, the gap increased with the particle size. As depicted, each group of particles appeared to have a log-normal distribution, which the original mixture before the sub-division also has (not shown).

Table 1

Gap size distribution between particles obtained from the SEM image of each sample.

Sample	Mean (μm)	Minimum (μm)	Standard deviation (μm)
$\alpha\text{-Al}_2\text{O}_3$ (S)	4.30	0.55	3.22
$\alpha\text{-Al}_2\text{O}_3$ (M)	4.73	1.12	2.37
$\alpha\text{-Al}_2\text{O}_3$ (L)	9.87	3.52	4.15
sea sand (S)	3.04	0.77	0.94
sea sand (M)	4.10	1.05	1.09
sea sand (L)	10.87	4.26	4.44
KIT-6 (S)	2.07	0.59	0.78
KIT-6 (M)	4.23	2.14	0.97
KIT-6 (L)	8.43	3.16	3.15

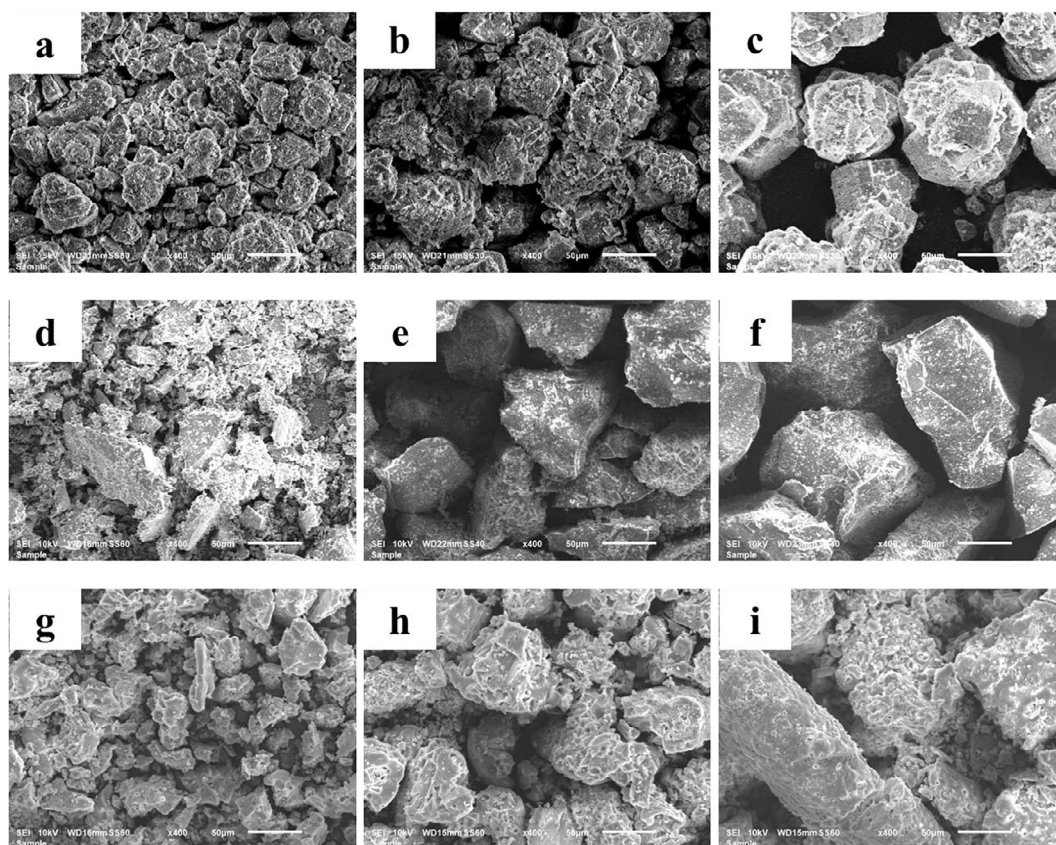


Fig. 1. SEM image of (a) fresh α - Al_2O_3 (S), (b) fresh α - Al_2O_3 (M), (c) fresh α - Al_2O_3 (L), (d) fresh sea sand (S), (e) fresh sea sand (M), (f) fresh sea sand (L), (g) fresh KIT-6 (S), (h) fresh KIT-6 (M), and (i) fresh KIT-6 (L).

3.2. Activity tests in the DBD plasma bed

As shown in Fig. 3, the packed beds showed the higher conversion level in all the cases than the conversion of blank test at the early stage of reaction due to the enhanced intensity of electric field between dielectric particles [30]. In Fig. 3a, the selectivities of C2 chemicals such as ethylene and acetylene were far higher in the packed-bed tests than those in the blank test. In contrast, the selectivity of ethane in the blank test was shown to be higher than those of packed-bed tests. In terms of yield, the unsaturated C2 chemicals in the packed-bed tests were produced more than those in the blank test as shown in Fig. 3b. Table S3 shows maximum experimental errors in packed-bed tests with several packing materials. The calculated maximum errors were relatively small and the biggest was 12.00%. The molar balances on hydrogen and carbon in each test were calculated in Table S1. Due to the high initial activity, significant amount of coke was generated and a few of carbon balances were measured less than 100%.

It was interesting to find that the conversion seemed to have its maximum when the middle-sized particles (size M) were used, irrespective of materials. The threshold electric potential difference between polarized dielectric particles can be estimated by employing a slightly modified calculation method from original Paschen's law, which can be used to estimate a breakdown voltage between electrodes. Based on the findings of plasma irradiation in packed-bed systems, we have developed a new concept of micro-electrodes between dielectric particles and we have found that the maximum conversion could be obtained when the M particles were used (see Appendix A.).

Fig. 4 illustrates the local microelectric field between particles and the propagation of streamers and microdischarges between the polarized microelectrodes [42,43]. In this Figure, microelectrodes are induced by an external electric field between packed dielectric particles. Due to the high voltage and the dielectric barrier, streamers and

microdischarges are generated [44,45]. Those streamers and microdischarges reach to the top surface of a particle, which is positively charged due to polarization. At the moment, the bottom surface is negatively charged. The top and bottom surfaces turn out to be anode-like and cathode-like surfaces, respectively [42]. This phenomenon starts from the particles near the external cathode and consecutively takes place from particle to particle to the direction of the opposite electrode [46]. When the streamers wrap around the dielectric particles, electrons are seeded from the bottom surface of the particles since the intensity of local electric field is enhanced due to photoionization. The seeded electrons cause another avalanche and launch new streamers [42,43]. At that moment, the nitrogen and the methane molecules are collided with the accelerated electrons and consequently the positively charged ions are generated. Under the enhanced electric field, the generated positive ions are accelerated to cathode-like surface and collide with the surface. This collision produces secondary electrons to sustain the streamers [11,42,47]. Therefore, the induced local electric field and the induced charged surface of particles can be viewed as microelectric field and microelectrodes, respectively. By following this scheme, we could successfully apply Paschen's equation in a modified form to the induced local microelectric field between adjacent particles as if those induced charged surfaces were external electrode (denoted micro-cathode and micro-anode in Fig. 4).

Through the experimental observation, we found that the maximum conversion of methane could be obtained by packing M particles. The gap distance between the M particles was in the range of 4–5 μm , which was observed in Fig. 2 and Table 2. According to the previous reports [34,48,49], a lower the breakdown voltage can lead to the higher conversion, which coincides well with our observation. Based on these two findings, we came up with an idea that we could successfully explain the experimental result by applying the Paschen's equation and the concept of microelectrodes to the gap between charged dielectric

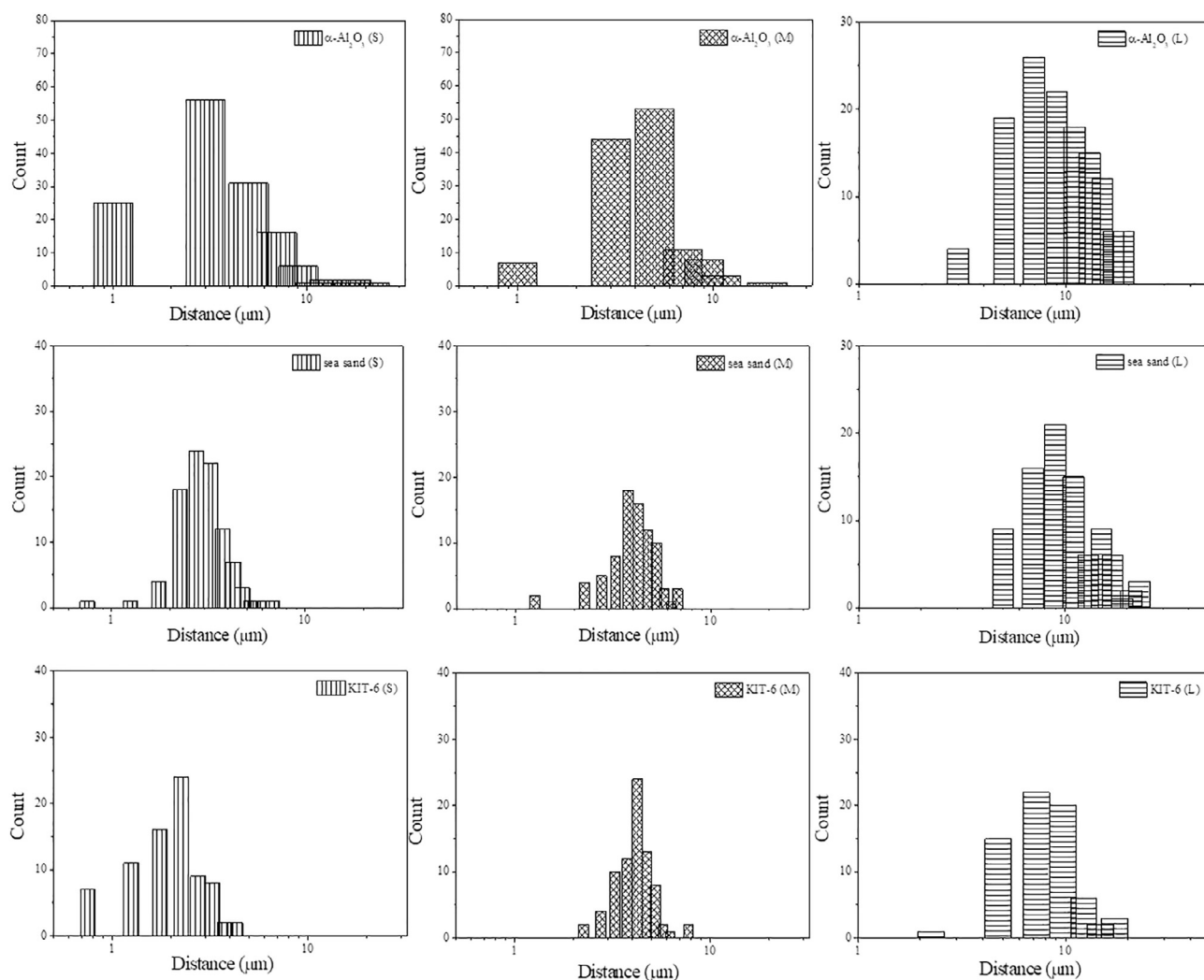


Fig. 2. Gap size distribution between particles obtained from the SEM image of each fresh sample.

particles. By combining the original Paschen's equation and the concept of microelectrodes, we proposed a modified Paschen's equation as in Appendix A. To evaluate the value of threshold electric potential difference, we estimated the value of γ by applying modified Paschen's equation and the gap at maximum conversion. The γ is generally known as very difficult to estimate exact value because it is affected by numerous factors [47]. In this work, we applied Paschen's equation for estimating secondary electron emission coefficient, γ , for all employed materials for the reaction. This application was based on our experimental observation, specifically methane conversion in the plasma bed

and each gap distance between the particles.

Table S2 shows various reaction performances on the non-oxidative methane coupling in a DBD plasma reactor reported by other researchers [33,50,51]. By comparing the results of the packed-bed tests with the blank tests, the increased CH_4 conversion and product selectivity were observed as shown in this study. The levels of conversion and selectivity seem to be dependent on reaction condition, species of materials, applied power and so on.

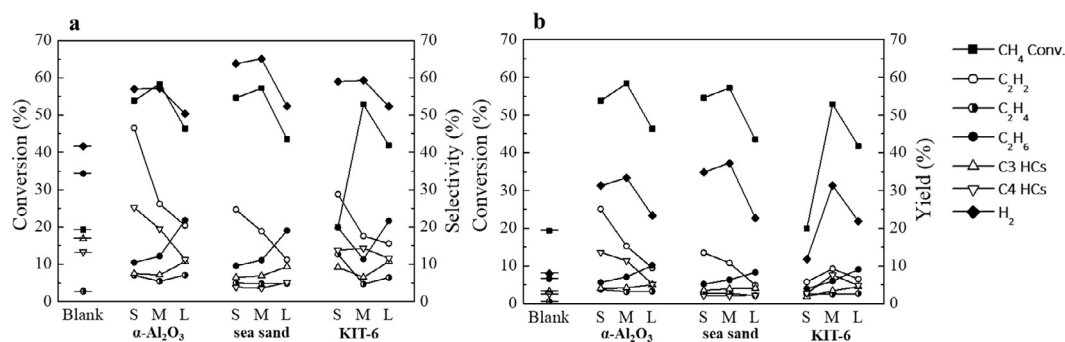


Fig. 3. Reaction performances when no particles (blank), $\alpha\text{-Al}_2\text{O}_3$, sea sand, and KIT-6 were used at TOS 60 min; (a) CH_4 conversion and product selectivity (b) CH_4 conversion and product yield.

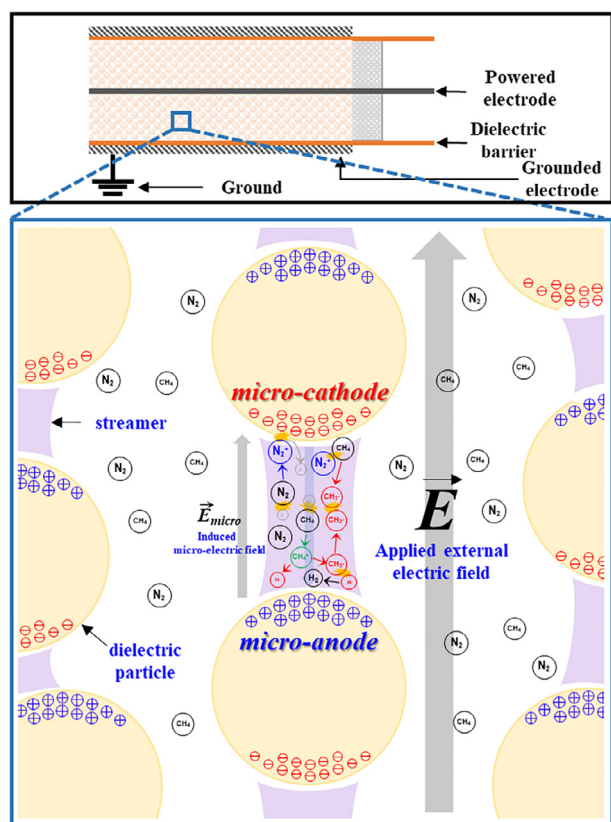


Fig. 4. Schematic representation of streamer and reactive intermediates between dielectric particles due to induced micro-electric field.

3.3. Effects of microdischarge on the performance

Fig. 5 shows the voltage-current profile in the each packed-bed test. The several current pulses were observed in all cases. These current pulses indicate the generation of microdischarges in the plasma bed [44,52]. Regarding the blank DBD plasma, the voltage-current profile is given in Fig. S5. Table 3 shows the average number and average intensity of microdischarge current pulses per one measured with voltage-current profile in the packed-bed DBD reactor. According to these Figures and Table, the increased number and intensity of microdischarges were observed in the cases of packed-bed tests compared with those in the case of blank test. These results coincided well with the previous report about the effect of the packed-bed [53].

Regarding the effects of size, the capability of charge transfer could be ascribed to the additive effects of the specific surface area and the capacitance of dielectric particles. Those two factors seem to be

proportional to the capability of charge transfer between the dielectric particles. The specific surface area decreases, whereas the capacitance of particle increases [42] as the size of particle increases. Therefore, the maximum capability of charge transfer could be obtained in the cases of M particles. In terms of chemical reaction, the capability of charge transfer could be translated as the activation capability of methane, indicating the methane conversion. In the previous section, the magnitude of threshold electric potential difference was found inversely proportional to the level of methane conversion. In addition, the threshold electric potential difference between the microelectrodes could be regarded as the breakdown voltage between electrodes in terms of the concept of microelectrodes. According to Jidenko et al. [54] and Ziomek et al. [55], the number of microdischarges increases as the breakdown voltage decreases. Therefore, the maximum number of microdischarges was observed in the cases of M particles, where maximum conversion was observed.

In addition, the intensity of microdischarge increased when the larger particles were packed in the bed as shown in Table 3. Regarding the microdischarge, Ohsawa et al. reported the effect of pellet size on the generation of microdischarges [56]. They pointed out that the employing larger pellet size reduces the number of microdischarges but intensifies the amount of charge transferred by an individual microdischarge. They claimed that the increased number of microdischarges by employing smaller sized particles was due to the increased number of contact point. In this study, however, it was observed in Fig. 5 that the number of valid microdischarges was greatest in the cases of employing M particles. Besides the number of contact points, the number of microdischarges seemed to have strong relation with electric property of dielectric particles such as capacitance, as previously explained. As a result, the maximum conversion was observed in the cases of M particles due to the greatest number of microdischarges with medium intensity.

In Table 2, the discharge power and the weight of packed particles were shown. As the size of particle decreased, the weight of particles as well as the discharge power seemed to increase in each material (α -Al₂O₃, sea sand, and KIT-6). The tendency of discharge power in the cases of sea sand samples appeared to be very slightly deviated at L particles, but it might be due to experimental error. It was understood that the increase in bed weight might require more discharge power to polarize the dielectric particles. In addition, Table 2 shows the breakdown voltage in the bed and the threshold electric potential difference between particles. The former was estimated by using Lissajous curve shown in Fig. S4, and the latter was computed by using the modified Paschen's equation to explain the potential difference to initiate streamer or discharge between dielectric particles (see Appendix A.). The breakdown voltage and the threshold electric potential difference showed their minima in the cases of M particles. This seems highly related to the fact that the conversion showed its maximum in the cases of M particles. The low threshold electric potential difference between

Table 2

Calculated discharge power by Q-V Lissajous method, calculated energy yields of total C2 and unsaturated C2 hydrocarbon products per discharge power, weight of particles in each bed, breakdown voltage in each bed, and calculated average threshold electric potential difference between particles.

Sample	Discharge power (W)	Y _{total} C2 (g/kWh)	Y _{unsaturated} C2 (g/kWh)	Weight of particles (g)	Breakdown voltage ^a (kV)	Threshold ΔV ^b (V)
α -Al ₂ O ₃ (S)	44.1	11.26	9.21	5.09	5.56	91.4
α -Al ₂ O ₃ (M)	43.5	8.61	5.98	5.06	5.53	90.9
α -Al ₂ O ₃ (L)	42.5	8.11	4.27	3.77	5.60	109
sea sand (S)	43.0	7.28	5.32	5.37	6.52	84.0
sea sand (M)	42.0	6.98	4.56	5.27	6.49	79.0
sea sand (L)	42.3	5.50	2.35	4.87	6.93	106
KIT-6 (S)	39.0	4.65	3.02	1.28	4.91	143
KIT-6 (M)	38.5	6.83	4.32	1.00	4.56	81.5
KIT-6 (L)	36.1	7.66	3.62	0.91	5.95	95.8

^a Measured from Lissajous Q-V plot (Fig. S4) [42].

^b Threshold electric potential difference (ΔV) between particles to initiate plasma discharges. Calculated from the modified Paschen's law (Appendix A.).

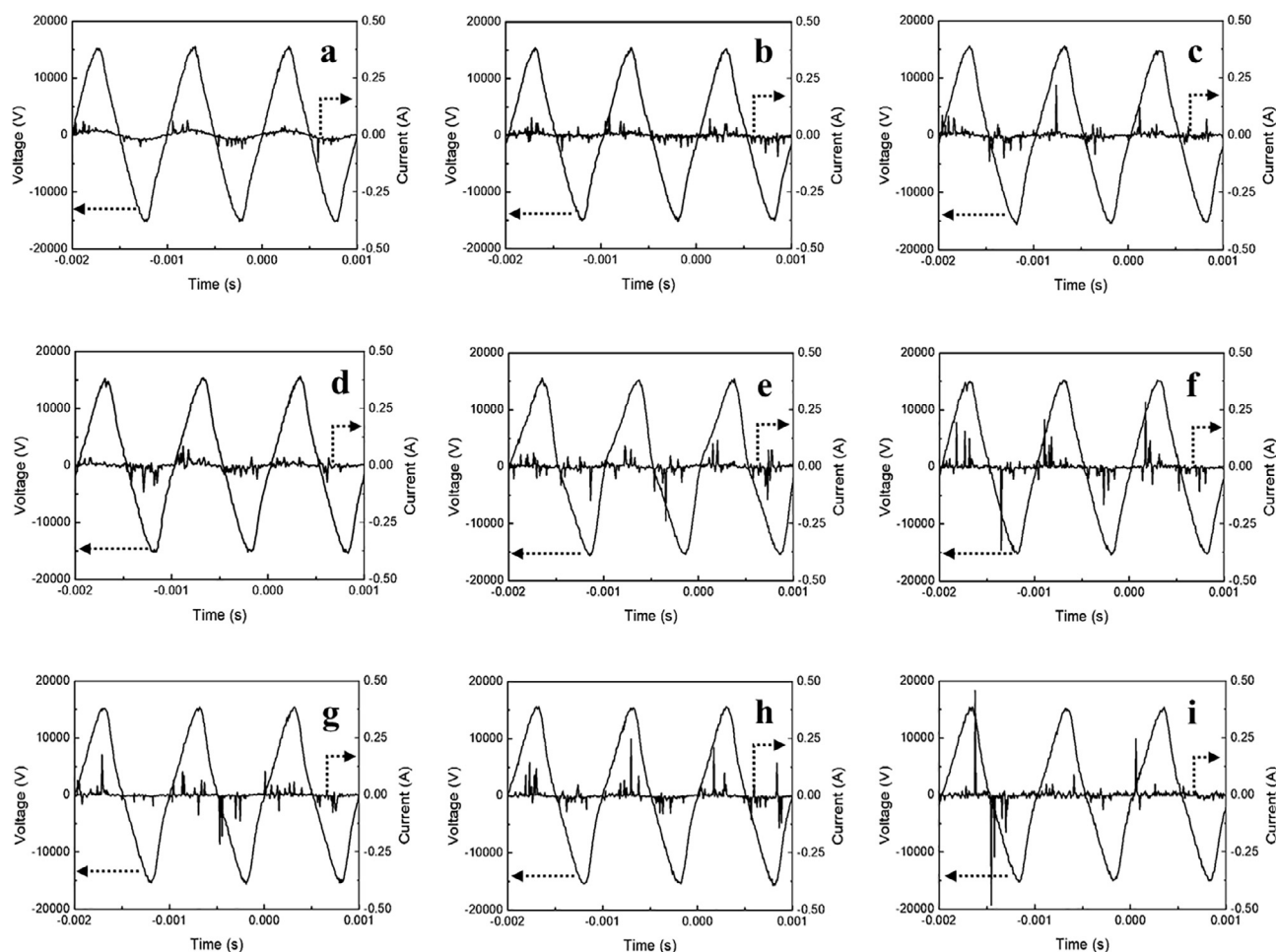


Fig. 5. Voltage-current profiles in the packed-bed DBD reactor with (a) α - Al_2O_3 (S), (b) α - Al_2O_3 (M), (c) α - Al_2O_3 (L), (d) sea sand (S), (e) sea sand (M), (f) sea sand (L), (g) KIT-6 (S), (h) KIT-6 (M), and (i) KIT-6 (L).

Table 3

Average number and average intensity of microdischarge current pulses per one measured with voltage-current profile in the packed-bed DBD reactor.

Sample	Average number of valid current pulses corresponding to microdischarges per one cycle (-)	Average intensity of microdischarge current pulses (mA)
Blank	3.3	39.0
α - Al_2O_3 (S)	10.0	47.5
α - Al_2O_3 (M)	13.0	54.0
α - Al_2O_3 (L)	9.3	61.8
sea sand (S)	12.0	48.9
sea sand (M)	13.0	67.5
sea sand (L)	11.0	94.8
KIT-6 (S)	12.3	63.5
KIT-6 (M)	13.3	73.7
KIT-6 (L)	6.0	85.9

the particles seemed to lead to the low breakdown voltage in the entire bed. This reduced breakdown voltage must have facilitated easier formation and more number of microdischarges in the bed as shown in Fig. 5 and Table 3, which resulted in higher converting capability.

3.4. Reaction pathway under the DBD plasma

Considering and reorganizing important reactions between intermediates from the references [30,57–64], a slightly modified reaction pathway is shown in Fig. 6. In this figure, the reaction pathway

describes methane activation, dehydrogenation, coupling, and chain-growth reactions as well.

Regarding the unsaturated C2 chemicals, the selectivity was shown to increase as the size of particles decreased. According to the mechanism by Liu et al. [30], the CH_x species dehydrogenated by plasma seemed to have two different routes to be coupled into unsaturated C2 chemicals. In the first route, methane is dehydrogenated to CH_3 radical and coupled with the other CH_3 radical to form C_2H_6 (ethane) or C_2H_5 species. A further dehydrogenation takes place stepwise and give C_2H_4 (ethylene) and C_2H_2 (acetylene). In the second route, the CH_3 radical further dehydrogenated to CH_2 or CH , which directly coupled into C_2H_4 and C_2H_2 , respectively.

For S particles, the total hydrocarbons selectivity (selectivity for C2 - C4) was found to be the highest. It might result from the highest specific surface area (highest surface to volume ratio for the smallest particles in the cases of nonporous materials such as α - Al_2O_3 and sea sand particles). This was also valid for highly porous KIT-6 particles. The surface area was measured by BET method and shown in Table S4. In general, the specific area increases as the size of particle decreases [65]. Also, Fig. S2 shows N_2 physisorption results of fresh KIT-6 in terms of (a) isotherm, (b) BJH pore size distribution. The specific surface area is proportional to the amount of surface oxygen ion vacancy sites, which are named V-centers and highly related to the generation of methyl radicals (CH_3). According to Liu et al. [59], when electronically excited states return to the ground states, energy is emitted in the form of electromagnetic radiation. Such radiation accounts for the ultraviolet to visible emissions of the gas discharge, and the V-center is formed due to the irradiation [60–62]. The methyl radicals can be formed by

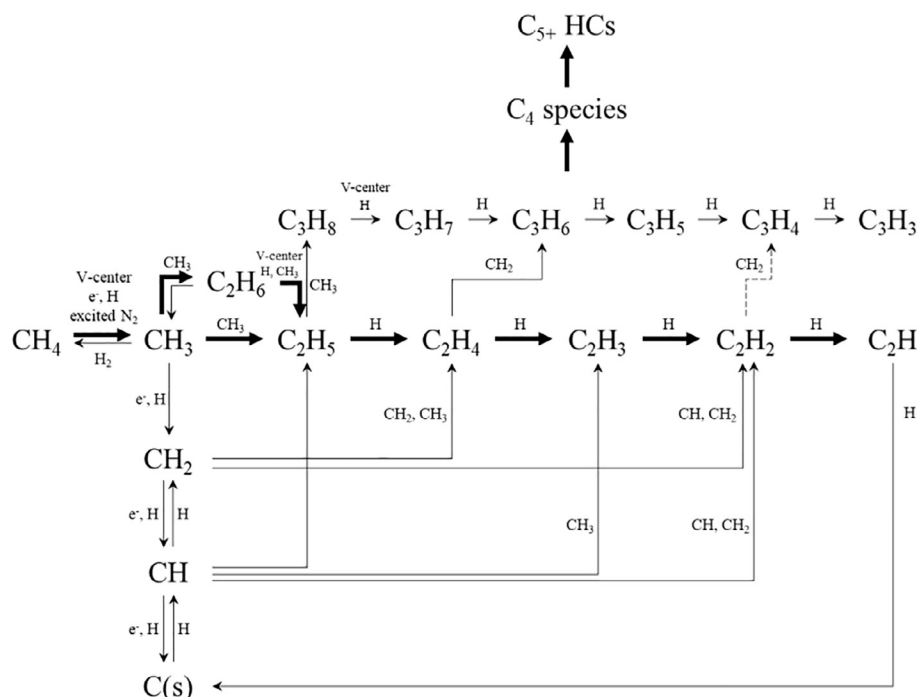


Fig. 6. Proposed reaction pathway describing methane activation, dehydrogenation, coupling and chain-growth reaction. The C_4 and C_{5+} indicate the hydrocarbon molecules having 4 carbon atoms, and the hydrocarbon molecules having more than 5 carbon atoms, respectively.

interaction with the V-center and methane. According to Ozin et al., the V-center photoactivated by UV irradiation plays a role to dehydrogenate alkane through hydrogen abstraction [60], and a further dehydrogenation can facilitate the formation of unsaturated forms hydrocarbons from saturated hydrocarbons, i.e., ethylene from ethane. This effect of V-center seems very similar to a catalyst. However, the V-center is thought to be an initiator generating radicals rather than a traditional catalyst.

Besides, the decreased fraction of void space due to the small size particles turned out to be a denser environment and a higher pressure. Under the more compressed condition, the number of effective collisions between intermediate radicals must have been increased. Considering very short lifetimes of radicals, the small gap distance might have helped increase the number of effective collisions avoiding termination without chain-growth.

As a result, the unsaturated hydrocarbons selectivity as well as the total hydrocarbons selectivity in the cases of S particles was found to be the highest among the 3 different sizes (S, M, and L) regardless of the kind of material ($\alpha\text{-Al}_2\text{O}_3$, sea sand and KIT-6). This was also valid for either practically nonporous or highly porous material.

If we look into the phenomena in the cases of the small size

particles, it seemed that the dehydrogenated species such as CH_2 and CH had higher probability to collide with each other and with their kinds, and be subsequently coupled into unsaturated C_2 chemicals. In contrast, if the size of particles was large (L) and the space between the particles was also large, the dehydrogenation seemed to occur more frequently than the coupling, which resulted in additional carbon deposition. The increased amount of carbon deposition due to the dehydrogenation seemed to be the result of increased capacitance of large particles. As observed in Fig. 5, the intensity of discharges between L particles was increased and it has been known to increase with capacitance of particles [42] and this led to the amount of charge transferred by an individual microdischarge was increased [56], although the number of discharges was decreased due to decreased specific surface area in the cases of L particles.

Due to the large size, the specific surface area is relatively small compared with smaller particles. This is directly related to the number of V-centers. Because of the relatively small number of V-centers, the amount of ethylene from ethane at V-centers seemed to be smaller than that in the cases of smaller particles. In addition, the radicals had relatively low possibility to collide effectively for coupling. Instead, quite a few methyl radicals seemed to have followed the dehydrogenation

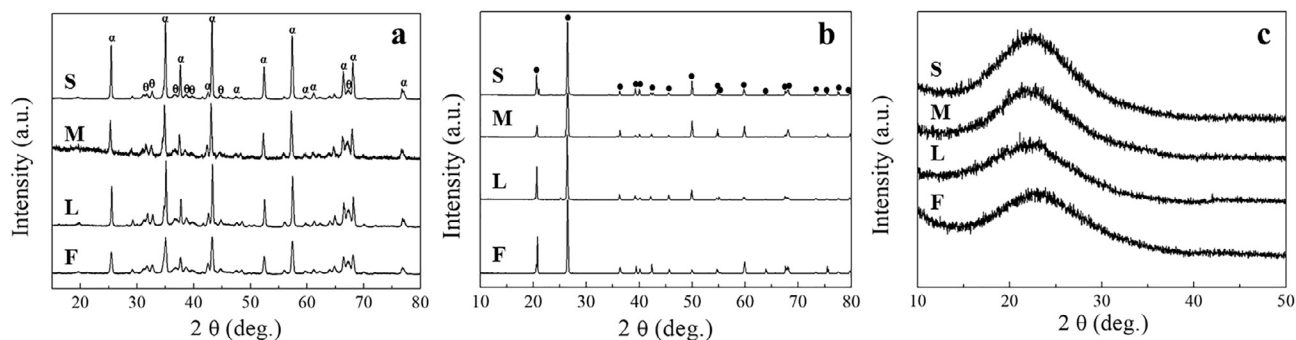


Fig. 7. XRD patterns of (a) spent $\alpha\text{-Al}_2\text{O}_3$, (b) spent sea sand, and (c) spent KIT-6 samples. (S), (M), and (L) denote the size of each sample, and (F) denotes the original fresh sample. α , θ , and \bullet denote XRD peak of $\alpha\text{-Al}_2\text{O}_3$, $\theta\text{-Al}_2\text{O}_3$, and quartz, respectively.

route (the 2nd route in the pre-described mechanism) and turned out to be carbon deposition. Fig. S6 shows reaction performances of each test at TOS 380 min. Due to the carbon deposition on the samples, significant decreases in CH_4 conversion and product yield were observed, while the conversion and the product yield changed very slightly in the case of blank test. The carbon deposition and its analysis will be dealt in the later section with TGA and DTA.

3.5. Analysis results after plasma coupling reaction

At the pre-described mechanism of microdischarge generation between the particles, the generated C_xH_y radicals might collide with the dielectric particle surface. Due to these collisions, the radicals were presumably attached to the surface and left to form a carbonaceous deposition, which was observed in the spent samples. According to Table S1, the molar balances on carbon in a few samples were quite lower than 100% at the initial stage (TOS 60 min) comparing to the data of TOS 300 min. These results indicate that this kind of carbonaceous deposition seemed to be generated dominantly at the initial stage.

Fig. 7 shows the results of WAXRD (wide angle X-ray diffraction spectroscopy) for spent samples and fresh original samples (not size-controlled). The alumina samples in Fig. 7a showed that the most dominant phase in the original fresh sample (F) was α -phase, but a small fraction of θ -phase was also detected in all the samples. In Fig. 7b, the quartz phase was clearly seen in the fresh and the spent samples. The XRD result in Fig. 7c showed that all the fresh and spent KIT-6 samples were found amorphous. As shown, the phase and the crystallinity of each sample (alumina and sea sand samples) did not change after the plasma coupling reaction. Regarding the KIT-6, the SAXS experiment was utilized to verify the structural stability after the reaction. All the fresh samples showed highly ordered mesoporous structure known as Ia3d bicontinuous phase (Fig. S3 a, c, and e). After the plasma coupling reaction, they successfully retained their highly ordered structure, and the spectrum of each spent sample (b, d, and f) showed no significant alterations. The spectrum intensity of spent KIT-6 (L) seemed to be a little bit weakened possibly due to carbon deposition.

Fig. 8 shows the TEM images of fresh (a-c) and spent samples (d-f). The structural changes were barely observed in the spent samples. In

Fig. S7, the particle surface of each spent sample was observed by the SEM images. The changes on the surface of spent samples could be observed and the amount of deposition seemed to be increased as the particle size increased, although the deposited elements such as carbon were hardly identified with these images. Fig. S8 shows the results of the TEM imaging analyses with EDS of spent samples. In the cases of spent α - Al_2O_3 (a) and spent sea sand (b), the carbon deposition on the surface did not seem to be significant, whereas in the case of spent KIT-6 (c), the significant amount of carbon was observed on the spent KIT-6.

To assess the carbon deposition, the analyses of TGA and DTA were conducted for the spent samples. As shown in Fig. 9 and Table 4, the amount of carbon deposition was increased as the size of particles increased. It was understood that the amount of carbon deposition was increased since the increased intensity of microdischarges for large particles accelerated dehydrogenation.

As shown in the result of TG/DTA, two major peaks were observed at around 400 °C and at 500–600 °C indicating two different carbon species were deposited. From the XRD results, most of the carbon species were found amorphous, and may be easily removed through traditional oxidation treatments or plasma irradiation techniques [66]. Especially, the amount of coke in the highly porous KIT-6 was significantly greater than those in the spent α - Al_2O_3 and sea sand samples. This was possibly due to the fact that the carbon species might have grown into the numerous pores of KIT-6 samples as the reaction proceeded.

Fig. 10 shows the result of FT-IR observation. The similar species of carbon were detected in all the spent samples. At 2850 and 3000 cm^{-1} , CH_3 stretch vibration mode was observed [67]. The peak at 2200 cm^{-1} may be assigned to the carbon-carbon triple bond stretching mode [68], or cyano group ($-\text{CN}$) [69] due to chemical reaction between CH_4 and N_2 [57]. The peaks at 1640 cm^{-1} and 1463 cm^{-1} can be ascribed to the carbon-carbon double bond stretching mode [70], and the asymmetric C-H bending mode of methylene group in a long aliphatic chains [71], respectively. Considering all these features, the carbon species in the FT-IR spectra could be classified as a carbon deposition having long-chain hydrocarbons.

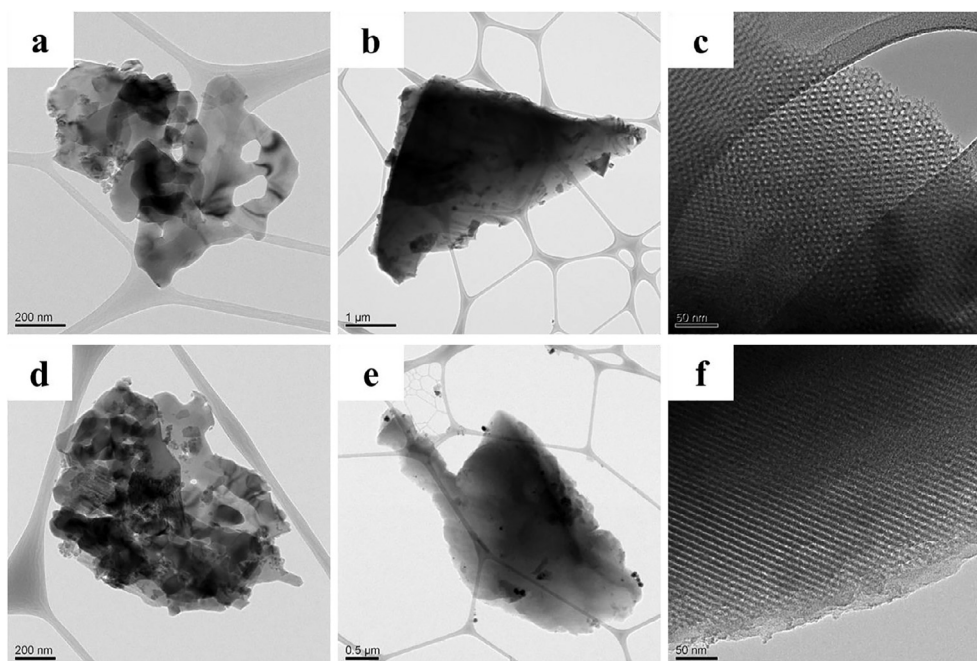


Fig. 8. TEM image of (a) fresh α - Al_2O_3 , (b) fresh sea sand, (c) fresh KIT-6. (d) spent α - Al_2O_3 , (e) spent sea sand, and (f) spent KIT-6.

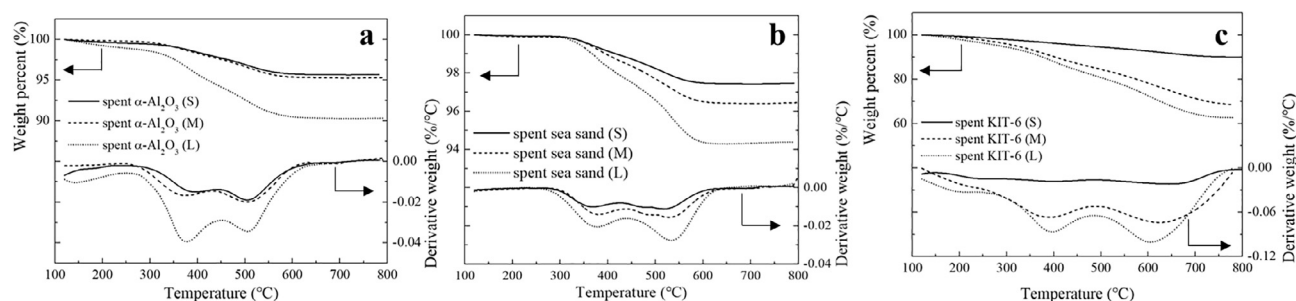


Fig. 9. TG/DTA results of (a) spent α - Al_2O_3 , (b) spent sea sand, and (c) spent KIT-6 samples.

Table 4

TG/DTA results of spent α - Al_2O_3 , spent sea sand, and spent KIT-6 samples.

Sample	Weight loss (%)	lower DTA peak (°C)	higher DTA peak (°C)
α - Al_2O_3 (S)	4.32	387	505
α - Al_2O_3 (M)	4.67	373	506
α - Al_2O_3 (L)	9.67	378	506
sea sand (S)	2.52	370	518
sea sand (M)	3.54	379	529
sea sand (L)	5.61	379	533
KIT-6 (S)	9.95	396	648
KIT-6 (M)	31.3	395	624
KIT-6 (L)	37.3	398	606

4. Conclusions

We have found that the methane conversion was not monotonically increased as the size of particles was decreased. Instead, the conversion was found to have its maximum in microscale range. The gap distance between dielectric particles was determined by the size of particle, which was experimentally shown. The gap distance at maximum conversion was observed experimentally, and this result was further analyzed by employing the concept of microelectrodes. The minimum threshold electric potential difference for the maximum conversion could be computed by the modified Paschen's equation.

Appendix A. Application of the modified Paschen's equation.

As explained in the manuscript, the induced charged surfaces of adjacent particles can act as microelectrodes, between which microdischarges are generated. If the gap between particles is focused on, the threshold electric potential difference to initiate the discharges between the microelectrodes can be substituted for the minimum breakdown voltage in the original form of Paschen's law [47], usually applied to an entire packed-bed to compute breakdown voltage between the external electrodes. Based on the concept of microelectrodes between dielectric particles, the modified Paschen's equation is given as follows.

Through the experiments with different sizes of particles, it was found that the selectivity of hydrocarbons could be controlled by adjusting the size of particles without catalysts, regardless of the porosity and the kind of material. Besides, the performance seemed to be also influenced by the dielectric constant, the morphology of particles and so on.

In the cases of highly porous dielectric particles, the amounts of carbon deposition were significant. The carbon species seemed to be deposited inside the pores.

In terms of hydrocarbons yield, the performance in α - Al_2O_3 -packed bed was very high, whereas the least amount of coke was produced in sea sand-packed bed. As the size of particles increased, the dehydrogenation seemed accelerated due to the increased intensity of microdischarges, and the amount of carbon deposition was increased accordingly.

Acknowledgments

This work was supported by the National Research Foundation of Korea (NRF), grant funded by the Korean Government (NRF-2016R1A2B4011717), and Human Resources Program in Energy Technology of the Korea Institute of Energy Technology Evaluation and Planning (KETEP), granted financial resource from the Ministry of Trade, Industry & Energy, Republic of Korea. (No. 20174010201150).

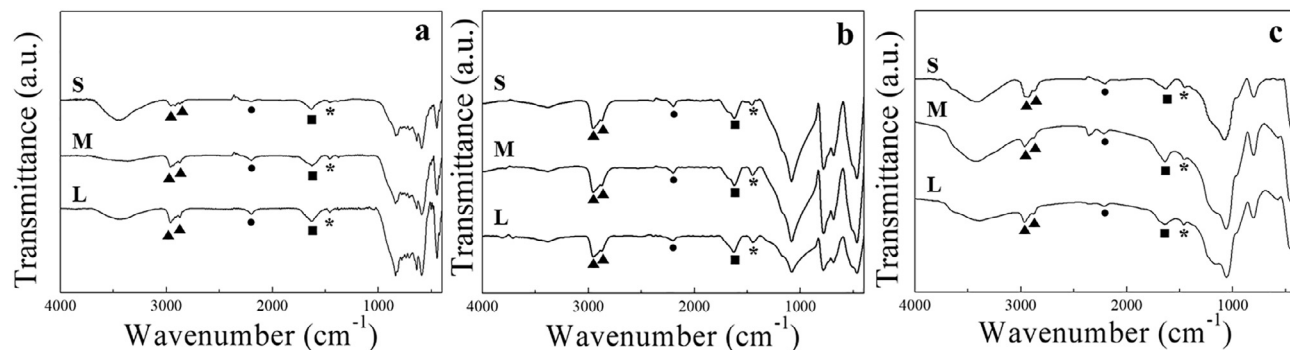


Fig. 10. FT-IR spectra of spent samples; (a) α - Al_2O_3 (b) sea sand (c) KIT-6. (S), (M), and (L) denote the size of each sample. \blacktriangle , \bullet , \blacksquare , and $*$ denote CH_3 stretch vibration mode, $\text{C}\equiv\text{C}$ stretching mode or cyano group, $\text{C}=\text{C}$ stretching mode, and asymmetrical C-H bending mode of methylene groups in a long aliphatic chain, respectively.

$$\ln\left(1 + \frac{1}{\gamma}\right) = A \cdot p d_{\text{micro}} \cdot \exp\left(-\frac{B p d_{\text{micro}}}{\Delta V_{B,\text{micro}}}\right)$$

or

$$\Delta V_{B,\text{micro}} = \frac{B p d_{\text{micro}}}{\ln(p d_{\text{micro}}) + \ln\left[\frac{A}{\ln\left(1 + \frac{1}{\gamma}\right)}\right]}$$

where $\Delta V_{B,\text{micro}}$ is the threshold electric potential difference between micro-electrodes to initiate plasma discharges.

At 298 K, the ionization characteristic constants A and B for pure methane [11] and nitrogen [72] are as follows. The more details for A and B can be found at Nomenclature section in this file.

$$A_{\text{N}_2} = 10 \text{ torr}^{-1} \cdot \text{cm}^{-1}, B_{\text{N}_2} = 310 \text{ V} \cdot \text{torr}^{-1} \cdot \text{cm}^{-1}, \text{ and}$$

$$A_{\text{CH}_4} = 7.3 \text{ torr}^{-1} \cdot \text{cm}^{-1}, B_{\text{CH}_4} = 191 \text{ V} \cdot \text{torr}^{-1} \cdot \text{cm}^{-1}$$

The arithmetic average values were used for A and B constants according to the prescribed composition in the experimental section and the values are as follows.

$$A_{\text{avg}} = 8.7 \text{ torr}^{-1} \cdot \text{cm}^{-1}, \text{ and } B_{\text{avg}} = 251 \text{ V} \cdot \text{torr}^{-1} \cdot \text{cm}^{-1}$$

The pressure was ambient pressure during the reactions.

Secondary electron emission coefficient, γ , is a function of E/p , i.e., the intensity of electric field divided by pressure [47,73]. The value of this parameter is very difficult to find because it can be varied depending on local electric field [11], kind of material, state of particles [47]. The value in a packed-bed is expected to be higher than that in a blank reactor, where the value usually ranges from 0.1 to 0.2 [74,75].

To find the equation for the minimum threshold electric potential difference, a differentiation of potential difference with respect to the gap distance was performed. The resulting equation is as follows.

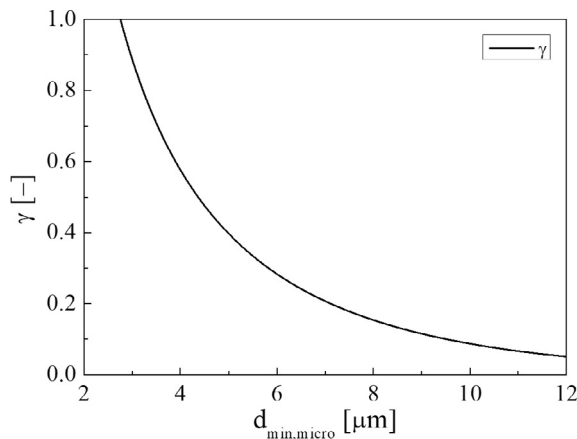
$$d_{\text{min,micro}} = \frac{e}{A p} \cdot \ln\left(1 + \frac{1}{\gamma}\right) \quad (\text{where, } e = \exp(1))$$

or

$$\gamma = \frac{1}{\exp\left(\frac{A p d_{\text{min,micro}}}{e}\right) - 1}$$

Putting the values of parameters will give the following equation and curve.

$$\gamma = \frac{1}{\exp\left(\frac{d_{\text{min,micro}}/\text{cm}}{0.000411}\right) - 1}$$



As explained in the manuscript, the maximum conversion was observed at the minimum threshold electric potential difference, values of γ for each material are estimated by using $d_{\text{min,micro}}$.

Mean gap distances of $\alpha\text{-Al}_2\text{O}_3$ (M), sea sand (M) and KIT-6 (M) were 4.73, 4.10, and 4.23 μm , respectively. We assume that the $d_{\text{min,micro}}$ for each material is very close to the gap distance of M-sized particles. Based on this, the γ values can be found as follows.

$$\gamma_{\alpha\text{-Al}_2\text{O}_3} = 0.463,$$

$$\gamma_{\text{sea sand}} = 0.584, \text{ and}$$

$$\gamma_{\text{KIT-6}} = 0.556$$

Finally, the equations for threshold electric potential difference are given.

$$\Delta V_{B,\text{micro},\alpha\text{-Al}_2\text{O}_3} = \frac{191,000 \cdot d_{\text{micro}}/\text{cm}}{\ln(d_{\text{micro}}/\text{cm}) + 8.65} [\text{V}]$$

$$\Delta V_{B,\text{micro},\text{sea sand}} = \frac{191,000 \cdot d_{\text{micro}}/\text{cm}}{\ln(d_{\text{micro}}/\text{cm}) + 8.79} [\text{V}], \text{ and}$$

$$\Delta V_{B, \text{micro, KIT-6}} = \frac{191,000 \cdot d_{\text{micro}}/\text{cm}}{\ln(d_{\text{micro}}/\text{cm}) + 8.76} [\text{V}]$$

Appendix B. Supplementary data

Supplementary data associated with this article can be found, in the online version, at <https://doi.org/10.1016/j.cej.2018.09.057>.

References

- [1] K.-S. Ha, G. Kwak, K.-W. Jun, J. Hwang, J. Lee, Ordered mesoporous carbon nanochannel reactors for high-performance Fischer-Tropsch synthesis, *Chem. Commun.* 49 (2013) 5141–5143.
- [2] M. Stöcker, Methanol-to-hydrocarbons: catalytic materials and their behavior, *Microporous Mesoporous Mat.* 29 (1999) 3–48.
- [3] K. Klier, Methanol Synthesis, *Advances in Catalysis*, Elsevier, 1982, pp. 243–313.
- [4] T. Ogawa, N. Inoue, T. Shikada, Y. Ohno, Direct dimethyl ether synthesis, *J. Nat. Gas Chem.* 12 (2003) 219–227.
- [5] A. Hwang, M. Kumar, J.D. Rimer, A. Bhan, Implications of methanol disproportionation on catalyst lifetime for methanol-to-olefins conversion by HSSZ-13, *J. Catal.* 346 (2017) 154–160.
- [6] T. Forbath, Acetylene by the BASF process, *Petrol. Refiner.* 33 (1954) 160–165.
- [7] H. Gladish, How Huels make acetylene by DC Arc, *Hydrocarbon Process. Petrol. Refiner.* 41 (1962) 159–164.
- [8] G. Keller, M. Bhasin, Synthesis of ethylene via oxidative coupling of methane: I. Determination of active catalysts, *J. Catal.* 73 (1982) 9–19.
- [9] V. Fleischer, U. Simon, S. Parishan, M.G. Colmenares, O. Görke, A. Gurlo, W. Riedel, L. Thum, J. Schmidt, T. Risse, Investigation of the role of the Na₂WO₄/Mn/SiO₂ catalyst composition in the oxidative coupling of methane by chemical looping experiments, *J. Catal.* 360 (2018) 102–117.
- [10] E.V. Kondratenko, M. Baerns, Oxidative coupling of methane, *Handbook of Heterogeneous Catalysis* (2008).
- [11] A. Fridman, *Plasma Chemistry*, Cambridge University Press, 2008.
- [12] P.A. Christensen, Z.T. Mashhadani, A.H.B. Md Ali, M.A. Carroll, P.A. Martin, The production of methane, acetone, “Cold” CO and oxygenated species from isopropyl alcohol in a non-thermal plasma: an in-situ FTIR study, *J. Phys. Chem. A* 122 (2018) 4273–4284.
- [13] W.V. Siemens, Ueber die elektrostatische Induction und die Verzögerung des Stroms in Flaschendrähnen, *Ann. Phys.* 178 (1857) 66–122.
- [14] A. Fridman, L.A. Kennedy, *Plasma Physics and Engineering*, CRC Press, 2004.
- [15] K. Takashima, T. Kaneko, Ozone and dinitrogen monoxide production in atmospheric pressure air dielectric barrier discharge plasma effluent generated by nanosecond pulse superimposed alternating current voltage, *Plasma Sources Sci. Technol.* 26 (2017) 065018.
- [16] C. Norsic, J.-M. Tatibouët, C. Batiot-Dupeyrat, E. Fourré, Methanol oxidation in dry and humid air by dielectric barrier discharge plasma combined with MnO₂-CuO based catalysts, *Chem. Eng. J.* 347 (2018) 944–952.
- [17] X. Hu, G.-B. Zhao, J.-J. Zhang, L. Wang, M. Radosz, Nonthermal-Plasma Reactions of Dilute Nitrogen Oxide Mixtures: NO x-in-Argon and NO x + CO-in-Argon, *Ind. Eng. Chem. Res.* 43 (2004) 7456–7464.
- [18] H. Wedaa, M. Abdel-Salam, A. Ahmed, A. Mizuno, NO removal using dielectric barrier discharges in a multitrod reactor stressed by AC and pulsed high voltages, *IEEE Trans. Dielectr. Electr. Insul.* 18 (2011).
- [19] Q. Yu, Y. Gao, X. Tang, H. Yi, R. Zhang, S. Zhao, F. Gao, Y. Zhou, Removal of NO from flue gas over HZSM-5 by a cycling adsorption-plasma process, *Catal. Commun.* 110 (2018) 18–22.
- [20] D. Xie, Y. Sun, T. Zhu, L. Hou, X. Hong, Nitric oxide oxidation and its removal in mist by nonthermal plasma: Effects of discharge conditions, *Ind. Eng. Chem. Res.* 56 (2017) 11336–11343.
- [21] H. Ma, P. Chen, M. Zhang, X. Lin, R. Ruan, Study of SO₂ removal using non-thermal plasma induced by dielectric barrier discharge (DBD), *Plasma Chem. Plasma Process.* 22 (2002) 239–254.
- [22] D. Ighigeanu, D. Martin, E. Zissulescu, R. Macarie, C. Oproiu, E. Cirstea, H. Iovu, I. Calinescu, N. Iacob, SO₂ and NO_x removal by electron beam and electrical discharge induced non-thermal plasmas, *Vacuum* 77 (2005) 493–500.
- [23] A. Koutsospyros, S.-M. Yin, C. Christodoulatos, K. Becker, Destruction of hydrocarbons in non-thermal, ambient-pressure, capillary discharge plasmas, *Int. J. Mass Spectrom.* 233 (2004) 305–315.
- [24] A.M. Vandenbroucke, R. Morent, N. De Geyter, C. Leys, Non-thermal plasmas for non-catalytic and catalytic VOC abatement, *J. Hazard. Mater.* 195 (2011) 30–54.
- [25] M.F. Mustafa, X. Fu, Y. Liu, Y. Abbas, H. Wang, W. Lu, Volatile organic compounds (VOCs) removal in non-thermal plasma double dielectric barrier discharge reactor, *J. Hazard. Mater.* 347 (2018) 317–324.
- [26] A. Ozkan, T. Dufour, G. Arnoult, P. De Keyser, A. Bogaerts, F. Reniers, CO₂-CH₄ conversion and syngas formation at atmospheric pressure using a multi-electrode dielectric barrier discharge, *J. CO₂ Util.* 9 (2015) 74–81.
- [27] A. Rahmani, M. Nikraveh, Impact of argon in reforming of (CH₄ + CO₂) in surface dielectric barrier discharge reactor to produce syngas and liquid fuels, *Plasma Chem. Plasma Process.* 38 (2018) 517–534.
- [28] D. Yap, J.-M. Tatibouët, C. Batiot-Dupeyrat, Catalyst assisted by non-thermal plasma in dry reforming of methane at low temperature, *Catal. Today* 299 (2018) 263–271.
- [29] Q. Wang, H. Shi, B. Yan, Y. Jin, Y. Cheng, Steam enhanced carbon dioxide reforming of methane in DBD plasma reactor, *Int. J. Hydrog. Energy* 36 (2011) 8301–8306.
- [30] C.-J. Liu, R. Mallinson, L. Lobban, Nonoxidative methane conversion to acetylene over zeolite in a low temperature plasma, *J. Catal.* 179 (1998) 326–334.
- [31] G. Lombardi, G. Stancu, F. Hempel, A. Gicquel, J. Röpkke, Quantitative detection of methyl radicals in non-equilibrium plasmas: a comparative study, *Plasma Sources Sci. Technol.* 13 (2003) 27.
- [32] T. Nozaki, N. Muto, S. Kadio, K. Okazaki, Dissociation of vibrationally excited methane on Ni catalyst: part 2. Process diagnostics by emission spectroscopy, *Catal. Today* 89 (2004) 67–74.
- [33] P. Kasinathan, S. Park, W.C. Choi, Y.K. Hwang, J.-S. Chang, Y.-K. Park, Plasma-enhanced methane direct conversion over particle-size adjusted MO x/Al₂O₃ (M = Ti and Mg) catalysts, *Plasma Chem. Plasma Process.* 34 (2014) 1317–1330.
- [34] S. Xu, J.C. Whitehead, P.A. Martin, CO₂ conversion in a non-thermal, barium titanate packed bed plasma reactor: The effect of dilution by Ar and N₂, *Chem. Eng. J.* 327 (2017) 764–773.
- [35] K. Van Laer, A. Bogaerts, Improving the conversion and energy efficiency of carbon dioxide splitting in a zirconia-packed dielectric barrier discharge reactor, *Energy Technol.* 3 (2015) 1038–1044.
- [36] D. Mei, X. Zhu, Y.-L. He, J.D. Yan, X. Tu, Plasma-assisted conversion of CO₂ in a dielectric barrier discharge reactor: understanding the effect of packing materials, *Plasma Sources Sci. Technol.* 24 (2014) 015011.
- [37] T. Butterworth, R. Elder, R. Allen, Effects of particle size on CO₂ reduction and discharge characteristics in a packed bed plasma reactor, *Chem. Eng. J.* 293 (2016) 55–67.
- [38] A. Montoro-Damas, J.J. Brey, M.A. Rodriguez, A.R. Gonzalez-Elipe, J. Cotrino, Plasma reforming of methane in a tunable ferroelectric packed-bed dielectric barrier discharge reactor, *J. Power Sources* 296 (2015) 268–275.
- [39] D. Kim, G.-A. Park, J. Lim, K.-S. Ha, Effects of spatially restricted Ni nanocrystals within ordered mesopores on the production of syngas, *Chem. Eng. J.* 316 (2017) 1011–1025.
- [40] P.M.K. Reddy, B.R. Raju, J. Karupiah, E.L. Reddy, C. Subrahmanyam, Degradation and mineralization of methylene blue by dielectric barrier discharge non-thermal plasma reactor, *Chem. Eng. J.* 217 (2013) 41–47.
- [41] L. Huang, L. Xia, W. Dong, H. Hou, Energy efficiency in hydrogen sulfide removal by non-thermal plasma photolysis technique at atmospheric pressure, *Chem. Eng. J.* 228 (2013) 1066–1073.
- [42] N.Y. Babaeva, A.N. Bhoj, M.J. Kushner, Streamer dynamics in gases containing dust particles, *Plasma Sources Sci. Technol.* 15 (2006) 591.
- [43] W. Wang, H.-H. Kim, K. Van Laer, A. Bogaerts, Streamer propagation in a packed bed plasma reactor for plasma catalysis applications, *Chem. Eng. J.* 334 (2018) 2467–2479.
- [44] X. Tu, H.J. Gallon, M.V. Twigg, P.A. Gorry, J.C. Whitehead, Dry reforming of methane over a Ni/Al₂O₃ catalyst in a coaxial dielectric barrier discharge reactor, *J. Phys. D-Appl. Phys.* 44 (2011) 274007.
- [45] X. Tu, H.J. Gallon, J.C. Whitehead, Transition behavior of packed-bed dielectric barrier discharge in argon, *IEEE Trans. Plasma Sci.* 39 (2011) 2172–2173.
- [46] K. Van Laer, A. Bogaerts, How bead size and dielectric constant affect the plasma behaviour in a packed bed plasma reactor: a modelling study, *Plasma Sources Sci. Technol.* 26 (2017) 085007.
- [47] R. Arora, W. Mosch, *High Voltage and Electrical Insulation Engineering*, John Wiley & Sons, 2011.
- [48] N. Pinhão, A. Janeco, J. Branco, Influence of helium on the conversion of methane and carbon dioxide in a dielectric barrier discharge, *Plasma Chem. Plasma Process.* 31 (2011) 427–439.
- [49] E.L. Reddy, V. Biju, C. Subrahmanyam, Production of hydrogen and sulfur from hydrogen sulfide assisted by nonthermal plasma, *Appl. Energy* 95 (2012) 87–92.
- [50] S. Kudryashov, A. Ryabov, G. Shchyogoleva, A new approach to the non-oxidative conversion of gaseous alkanes in a barrier discharge and features of the reaction mechanism, *J. Phys. D-Appl. Phys.* 49 (2015) 025205.
- [51] A. Indarto, N. Coowanitwong, J.-W. Choi, H. Lee, H.K. Song, Kinetic modeling of plasma methane conversion in a dielectric barrier discharge, *Fuel Process. Technol.* 89 (2008) 214–219.
- [52] H.-H. Kim, J.-H. Kim, A. Ogata, Microscopic observation of discharge plasma on the surface of zeolites supported metal nanoparticles, *J. Phys. D-Appl. Phys.* 42 (2009) 135210.
- [53] H.L. Chen, H.M. Lee, S.H. Chen, M.B. Chang, Review of packed-bed plasma reactor for ozone generation and air pollution control, *Ind. Eng. Chem. Res.* 47 (2008) 2122–2130.
- [54] N. Jidenko, M. Petit, J.-P. Borra, Electrical characterization of microdischarges produced by dielectric barrier discharge in dry air at atmospheric pressure, *J. Phys. D-Appl. Phys.* 39 (2006) 281.
- [55] W. Ziomek, H. Moscicka-Grzesiak, Relation of breakdown voltage and prebreakdown microdischarge parameters in vacuum, *IEEE Trans. Electr. Insul.* 28 (1993)

- 481–487.
- [56] A. Ohsawa, R. Morrow, A. Murphy, An investigation of a dc dielectric barrier discharge using a disc of glass beads, *J. Phys. D-Appl. Phys.* 33 (2000) 1487.
- [57] A. Indarto, J.-W. Choi, H. Lee, H.K. Song, Effect of additive gases on methane conversion using gliding arc discharge, *Energy* 31 (2006) 2986–2995.
- [58] A. Majumdar, J.F. Behnke, R. Hippler, K. Matyash, R. Schneider, Chemical reaction studies in CH₄/Ar and CH₄/N₂ gas mixtures of a dielectric barrier discharge, *J. Phys. Chem. A* 109 (2005) 9371–9377.
- [59] C. Liu, A. Marafee, R. Mallinson, L. Lobban, Methane conversion to higher hydrocarbons in a corona discharge over metal oxide catalysts with OH groups, *Appl. Catal. A-Gen.* 164 (1997) 21–33.
- [60] G.A. Ozin, F. Hugues, Selective photoactivation of carbon-hydrogen bonds in paraffinic hydrocarbons. Dimerization of alkanes, *J. Phys. Chem.* 86 (1982) 5174–5179.
- [61] J. Vallayer, C. Jardin, D. Tréheux, Optical and dielectric behaviors of alumina after an electromagnetic irradiation, *Opt. Mater.* 16 (2001) 329–333.
- [62] Y. Inaki, H. Yoshida, T. Yoshida, T. Hattori, Active sites on mesoporous and amorphous silica materials and their photocatalytic activity: an investigation by FTIR, ESR, VUV – UV and photoluminescence spectroscopies, *J. Phys. Chem. B* 106 (2002) 9098–9106.
- [63] C.E. Canosa-Mas, M. Ellis, H.M. Frey, R. Walsh, The formation of C₃H₃ (propynyl) radicals in the reaction of CH₂ (1A₁) with acetylene, *Int. J. Chem. Kinet.* 16 (1984) 1103–1110.
- [64] D.F. Strobel, Chemistry and evolution of Titan's atmosphere, *Planet Space Sci.* 30 (1982) 839–848.
- [65] M. Borkovec, Q. Wu, H. Sticher, G. Degovics, P. Laggnier, Surface Area and Size Distributions of Soil Particles, Colloids in the Aquatic Environment, Elsevier, 1993, pp. 65–76.
- [66] M. Kim, J. Jeoung, J. Kim, K.-S. Ha, Regeneration of deactivated H-ZSM-5 for aromatization by dielectric barrier discharge plasma, submitted for publication (2018).
- [67] S. Nair, T. Nozaki, K. Okazaki, In situ Fourier transform infrared (FTIR) study of nonthermal-plasma-assisted methane oxidative conversion, *Ind. Eng. Chem. Res.* 46 (2007) 3486–3496.
- [68] A. Walker, T. Tighe, J. Stapleton, B. Haynie, S. Upilli, D. Allara, N. Winograd, Interaction of vapor-deposited Ti and Au with molecular wires, *Appl. Phys. Lett.* 84 (2004) 4008–4010.
- [69] R.R. Schumaker, E.M. Engler, Thiapen chemistry: synthesis of higher homologs of tetrathiafulvalene, *J. Am. Chem. Soc.* 102 (1980) 6651–6652.
- [70] P. Atkins, J. De Paula, *Atkins' Physical Chemistry*, New York (2006) 77.
- [71] S.-H. Wang, P.R. Griffiths, Resolution enhancement of diffuse reflectance ir spectra of coals by Fourier self-deconvolution: 1. CH stretching and bending modes, *Fuel* 64 (1985) 229–236.
- [72] A. Heylen, The relationship between electron—molecule collision cross-sections, experimental Townsend primary and secondary ionization coefficients and constants, electric strength and molecular structure of gaseous hydrocarbons, *Proc. Royal Soc. A, The Royal Society*, 2000, pp. 3005–3040.
- [73] F.A. Rizk, G.N. Trinh, *High Voltage Engineering*, CRC Press, 2014.
- [74] J.Y. Lee, H.W. Bae, H.J. Lee, J.P. Verboncoeur, The effect of power balance on the heating mode transition in micro-dielectric barrier helium glow discharges, *Plasma Sources Sci. Technol.* 23 (2014) 035017.
- [75] N.Y. Babaeva, M.J. Kushner, Self-organization of single filaments and diffusive plasmas during a single pulse in dielectric-barrier discharges, *Plasma Sources Sci. Technol.* 23 (2014) 065047.